


Mitofusin gain and loss of function drive pathogenesis in *Drosophila* models of CMT2A neuropathy

Najla El Fissi¹, Manuel Rojo², Aïcha Aouane¹, Esra Karatas², Gabriela Poliacikova¹, Claudine David², Julien Royet¹ & Thomas Rival^{1,*} 

Abstract

Charcot–Marie–Tooth disease type 2A (CMT2A) is caused by dominant alleles of the mitochondrial pro-fusion factor Mitofusin 2 (MFN2). To address the consequences of these mutations on mitofusin activity and neuronal function, we generate *Drosophila* models expressing in neurons the two most frequent substitutions (R94Q and R364W, the latter never studied before) and two others localizing to similar domains (T105M and L76P). All alleles trigger locomotor deficits associated with mitochondrial depletion at neuromuscular junctions, decreased oxidative metabolism and increased mtDNA mutations, but they differently alter mitochondrial morphology and organization. Substitutions near or within the GTPase domain (R94Q, T105M) result in loss of function and provoke aggregation of unfused mitochondria. In contrast, mutations within helix bundle 1 (R364W, L76P) enhance mitochondrial fusion, as demonstrated by the rescue of mitochondrial alterations and locomotor deficits by over-expression of the fission factor DRP1. In conclusion, we show that both dominant negative and dominant active forms of mitofusin can cause CMT2A-associated defects and propose for the first time that excessive mitochondrial fusion drives CMT2A pathogenesis in a large number of patients.

Keywords CMT2A; MFN2; mitochondrial fusion; mitofusin; peripheral neuropathy

Subject Categories Membrane & Intracellular Transport; Metabolism; Neuroscience

DOI 10.15252/embr.201745241 | Received 26 September 2017 | Revised 16 May 2018 | Accepted 23 May 2018 | Published online 13 June 2018

EMBO Reports (2018) 19: e45241

Introduction

Charcot–Marie–Tooth diseases (CMT), also called hereditary sensory motor neuropathies (HSMN), compose a heterogeneous family of genetically inherited human disorders affecting the

peripheral nervous system [1]. In opposition to CMT1, which results from myelin sheath loss, CMT2 is characterized by axonal alterations typically associated with reduced amplitude of nerve action potentials. The most severe and most frequent form of CMT2 is the subtype A (CMT2A) [1,2], which preferentially affects motor and sensory neurons with the longest axons, resulting in muscle atrophy, hand and feet deformities, and loss of perception in the distal part of the limb [2]. The onset of CMT2A ranges from the first to the fifth decade, the early forms being more severe and possibly associated with neurodegeneration [3–5]. Although few recessive forms have been described [6,7], CMT2A is mainly associated with dominant mutations scattered all along the *MFN2* gene coding sequence [2,3]. The mechanisms by which these *MFN2* mutations trigger neuronal dysfunctions remain unknown, and there is currently no cure for patients.

MFN2 encodes a mitochondrial outer membrane protein belonging to a family of highly conserved dynamin-related GTPases named mitofusins (MFNs) [8–10]. Fungi, nematodes, and insects encode a single or a single ubiquitously expressed MFN-homolog, such as Fzo1p in *Saccharomyces cerevisiae* or MARF in *Drosophila melanogaster*. Vertebrates encode two ubiquitously expressed homologs with high-sequence similarity (MFN1 and MFN2), but studies in mice indicate that MFN2 is the main MFN expressed in peripheral nerves [11]. MFNs support mitochondrial fusion, a GTP-dependent process that enables inter-mitochondrial exchanges essential for oxidative metabolism and results in mitochondrial elongation [12,13]. The precise role played by MFNs in membrane fusion and their mechanism of action are still speculative [14], as well as the consequences of CMT2A mutations on MFN function. Mitochondrial fusion is antagonized by mitochondrial fission, a process supported by another dynamin-related GTPase, DRP1 [15], and the balance between antagonizing fusion and fission reactions determines the overall morphology and dynamic properties of mitochondrial networks. Consequently, MFN inactivation results in mitochondrial fragmentation, through ongoing fission, and that of DRP1 provokes the appearance of hyper-fused mitochondria [10]. Of note, the GTPases involved in fusion and fission have been reported to play

¹ Aix Marseille University, CNRS, IBDM, Marseille, France

² University of Bordeaux, CNRS, Institut de Biochimie et Génétique Cellulaires (IBGC), UMR 5095, Bordeaux, France

*Corresponding author. Tel: +33 491 26 92 42; Fax: +33 491 69 89 77; E-mail: thomas.rival@univ-amu.fr

additional roles in other cellular processes, including apoptotic outer membrane permeabilization, interactions between endoplasmic reticulum and mitochondria, and coenzyme Q maintenance [8,10,16].

A tight regulation of the mitochondrial fusion/fission balance appears crucial to sustain neuronal activity. Indeed, mitochondrial fragmentation was linked to different neurodegenerative processes, and fission inhibitors were shown to provide neuroprotection *in vitro* and *in vivo* [17,18]. In addition, mutations in fusion and fission factors were associated with neurological disorders (*OPA1*: optic atrophy; *DRP1*: microcephaly, optic atrophy; *MFF*: Leigh-like encephalopathy, neuropathy) including CMT (*GDAP1*/CMT2K and CMT4A) [8,19,20]. While studies in animal models revealed that *DRP1* inactivation alters mitochondrial distribution in neurites [21] leading to mitochondrial depletion at synapses [22], the roles of mitochondrial fusion and MFNs in neurons are poorly documented. In mouse, *MFN2* knockout die at midembryogenesis [13] and neuronal-specific knockout [23–25] trigger severe neurological defects and neurodegeneration. These models confirm the requirement of *MFN2* and the relevance of mitochondrial fusion for neuronal function, but do not mimic the specific alterations of peripheral sensorimotor nerves observed in CMT2A patients. The study of transgenic mice expressing *MFN2* mutations associated with CMT2A revealed animals with locomotor defects associated with axonal loss [26], or alterations of axonal width [27,28]. However, the origin of these neuronal alterations and their link with altered MFN activity remains unknown. Indeed, the sole available *in vivo* analysis of mitochondria in CMT2A mouse models was limited and only showed a distal accumulation of mitochondria in peripheral nerves [27].

To advance our understanding of CMT2A pathogenesis, we developed four *in vivo* models of CMT2A by expressing different pathogenic MFN mutations in neurons of transgenic *Drosophila*. We chose to model the two most frequent substitutions, *R94Q* and *R364W*, identified in more than 25 patients each (Appendix Table S1 and [2]) and two further alleles, *L76P* and *T105M* [2], that localize to similar domains of MFN (Figs 1 and EV1). Mutations of the R94 and R364 residues are associated with severe early forms of CMT2A and, in some patients, to optic atrophy, a disease condition referred as CMT6/HSNMIV [4,29,30]. Of note, despite their high prevalence, mutations of the R364 residue have never been studied in cellular or animal models. We show that, when expressed in wild-type fly neurons, the four CMT2A-mimetic alleles are dominant and induce severe locomotor deficits. At the cellular level, the four mutations result in impaired mitochondrial functions and integrity, aberrant mitochondrial morphology and organization in neuronal soma, and mitochondrial depletion at neuromuscular junctions. Interestingly, however, MFN mutations at the edge or within the GTPase domain (corresponding to *R94Q* and *T105M*, Figs 1A and EV1) drive the clustering of unfused mitochondria, whereas those localizing to the adjacent helix bundle HB1 (corresponding to *R364W* and *L76P*, Figs 1A and EV1) provoke fusion-mediated mitochondrial enlargement.

Functional analysis of the human *MFN2* alleles in mouse cells confirmed that hMFN2-R94Q and T105M are fusion-incompetent and that, surprisingly, hMFN2-R364W or L76P are fusion-competent. We further demonstrate that enhanced fission by *DRP1* over-expression rescues the alterations of mitochondrial

morphology and distribution as well as locomotor deficit in the *R364W* fly model. Our findings demonstrate that, in at least two CMT2A alleles, including one of the most frequent, neuronal dysfunctions are provoked by increased mitochondrial fusion in neurons. We therefore propose that both deficient and excessive MFN activity drive CMT2A pathogenesis.

Results

Fly models of CMT2A develop neurological defects

To study the pathogenicity of the CMT2A alleles *R94Q*, *T105M*, *R364W*, and *L76P* in *Drosophila*, we introduced mutations homologous to these amino acid substitutions into the coding sequence of the fly MFN-homolog namely *marf* (Fig 1A and B). The four CMT2A alleles, plus a control *marf* wild-type cDNA, were placed under the transcriptional control of UAS activating sequences and inserted at the same genomic location (Fig 1B). To model CMT2A disease that is genetically defined as dominant, the transgenes were expressed in neurons of wild-type animals (Fig 1C) leading to similar expression level (Fig 1D). The low expression of the transgenes (Fig 1D) mimics well the situation in patient's tissue in which pathogenic and wild-type alleles are supposedly expressed at similar levels. To determine whether the CMT2A alleles were sufficient to impair neuronal activity in *Drosophila*, we analyzed the flies' locomotion. While neuronal expression of the *marf* wild-type transgene had no effect, the four CMT2A alleles impair locomotor capacity (Fig 1E). The locomotor performances of *R94Q^{like}*, *R364W^{like}*, and *L76P^{like}* flies were reduced by 95, 65, and 50%, respectively, and *T105M^{like}* animals display paralysis that prevents the hatching of most adult flies. These results demonstrate that all tested *marf* alleles carrying CMT2A mutations are dominant and pathogenic in *Drosophila*, leading to neurological alterations.

CMT2A fly models develop different alterations of mitochondrial morphology in neurons

Then, we analyzed the consequences of the CMT2A alleles on mitochondrial morphology by imaging living larval motor neurons that are easily accessible to *in vivo* microscopy. Consistent with increased mitochondrial fusion, expression of control *marf^{WT}* transgene increased mitochondrial length in neuronal cell bodies (Fig 2A–D), whereas knocking down *marf* resulted in mitochondrial fragmentation (*marf^{RNAi}*, Fig 2B–D). In contrast, in neurons expressing *R94Q^{like}* and *T105M^{like}*, most visible mitochondria were sequestered into one or few massive mitochondrial aggregates (Fig 2A and B, and Appendix Fig S1 *OK371-GAL4*, and Fig EV2B *elav-GAL4*) composed of a myriad of tightly packed mitochondria (Fig 2E). Interestingly, in neuronal cell bodies expressing *R364W^{like}* and *L76P^{like}*, the mitochondrial morphology was affected in a very different manner, with the presence of numerous large round shape mitochondria distributed throughout the cytoplasm among few long mitochondrial tubules (Fig 2A–C and F, and Appendix Fig S1 *OK371-GAL4*, and Fig EV2B *elav-GAL4*). Electron microscopy confirmed that the abnormal structures detected by fluorescence correspond to mitochondria

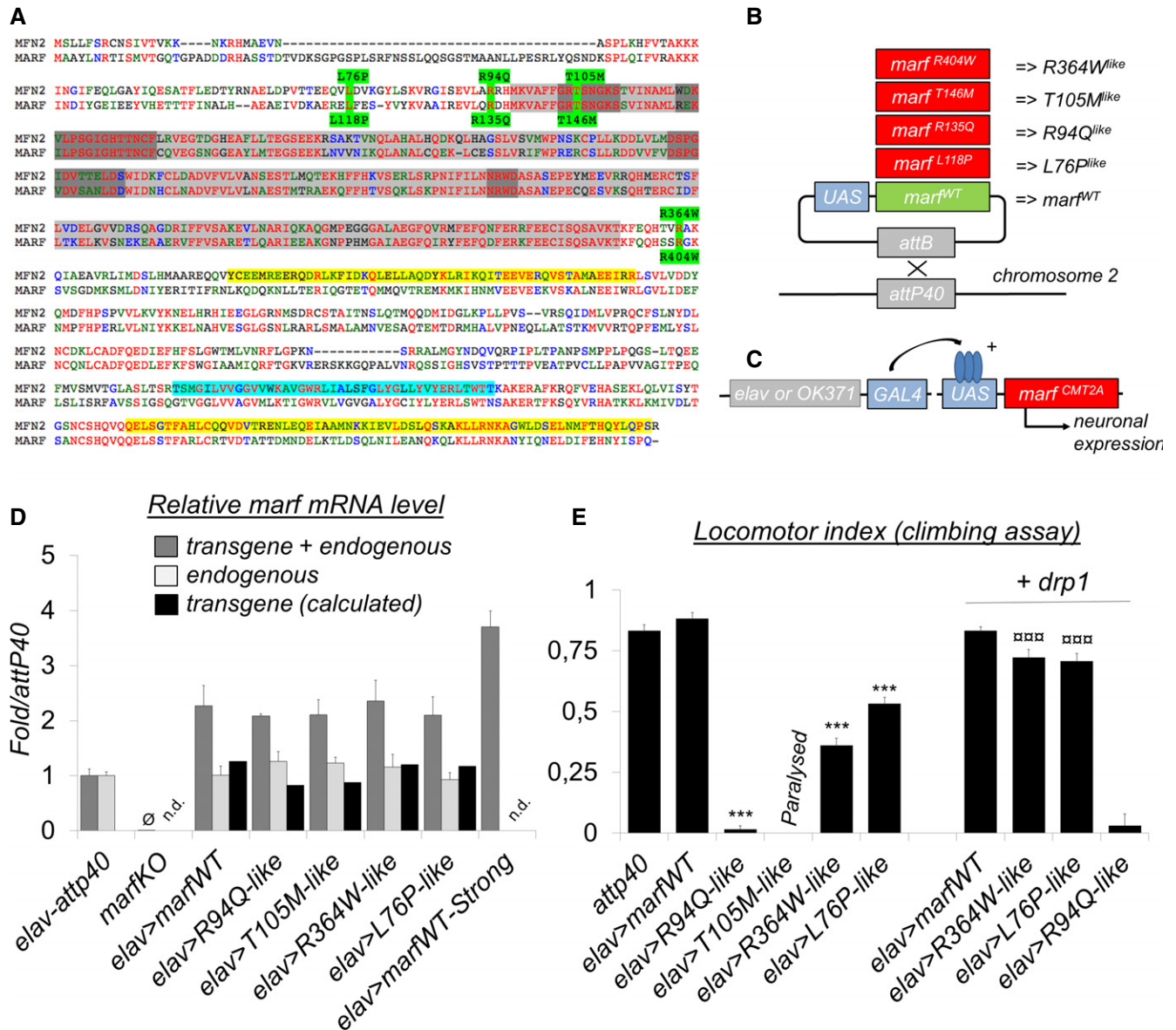


Figure 1. Neuronal expression of CMT2A-mimetic alleles triggers locomotor defects in flies.

- A** Sequence alignment of human MFN2 and *Drosophila* MARF. MFN2 mutations and homologous MARF residues (green), GTP-binding domain (light gray), GTP-binding motifs G1 to G4 (dark gray), coiled-coil/CC domains (yellow), and transmembrane/TM domains (cyan). R94 and T105 are, respectively, located at the edge and within the GTP-binding domain (position in folded structure see Fig EV1). L76 and R364, that appear distant in the MFN2 linear sequence, are in fact part of the same helix bundle (HB1) as shown in the folded structure (Fig EV1).
- B** We mutated the amino acids homologous to R94, T105, R364, and L76 in the coding sequence of *marf* to generate the R404Q, L118P, R135Q, and T146M substitutions (referred here as *R364W*^{like}, *L76P*^{like}, *R94Q*^{like}, and *T105M*^{like} for simplicity of interpretation), and each *marf* allele was placed under the transcriptional control of UAS activation sequences. As a control, we similarly generated a wild-type UAS-*marf* construct. The five *marf* transgenes were inserted at the *attP40* insertion site to insure similar genetic background and expression level.
- C** The expression of the UAS-*marf*^{CMT2A} alleles was specifically induced into the neurons of wild-type flies using the pan-neuronal driver *elav*-GAL4 which targets all central and peripheral neurons or the glutamatergic driver *OK371*-GAL4 which facilitates the imaging of motor neurons.
- D** qRT-PCR performed on larval nervous system extracts showing *marf* mRNA level relative to control (*elav*>*attp40*). "transgene + endogenous": The amplified sequence is present both in mRNAs encoded by UAS-*marf* transgenes and the endogenous *marf* gene. "endogenous": amplification of the 3'UTR region that is absent from mRNAs transcribed from UAS-*marf* transgenes. The level of "transgene" was calculated ("transgene+endogenous"-endogenous). (mRNA levels \pm SD represent the mean value for two independent mRNA extracts each obtained from 12 dissected larval brains). *marf*^{KO}: knockout of the *marf* endogenous gene deleting the whole coding sequence and abolishing mRNA expression (\emptyset : value close to 0) (Appendix Fig S2 for technical details). *marf*^{strong}: previously generated UAS-*marf* transgene [33] inserted at a different genomic location and leading to higher expression level than the UAS-*marf*^{WT} transgene described in this study.
- E** Result of negative geotaxis test (NGT). Flies were placed into a vertical column and tapped to the bottom to induce escape behavior. After 30 s, the flies reaching the top of the column (N_{top}) and the flies remaining at the bottom (N_{bot}) are counted to calculate a locomotor index (\pm SEM) defined as: $1/2 * (N_{total} + N_{top} - N_{bot}) / N_{total}$. Nine races involving three groups of 10 flies for each genotype. Mann-Whitney test results: *marf*^{WT} versus CMT2A alleles *** $P < 0.001$. *R364W*^{like} or *L76P*^{like} versus same condition + *drp1*: $\square\square\square\square P < 0.001$. "Paralysis": NGT not performed on *T105M*^{like} flies because these animals are completely paralyzed.

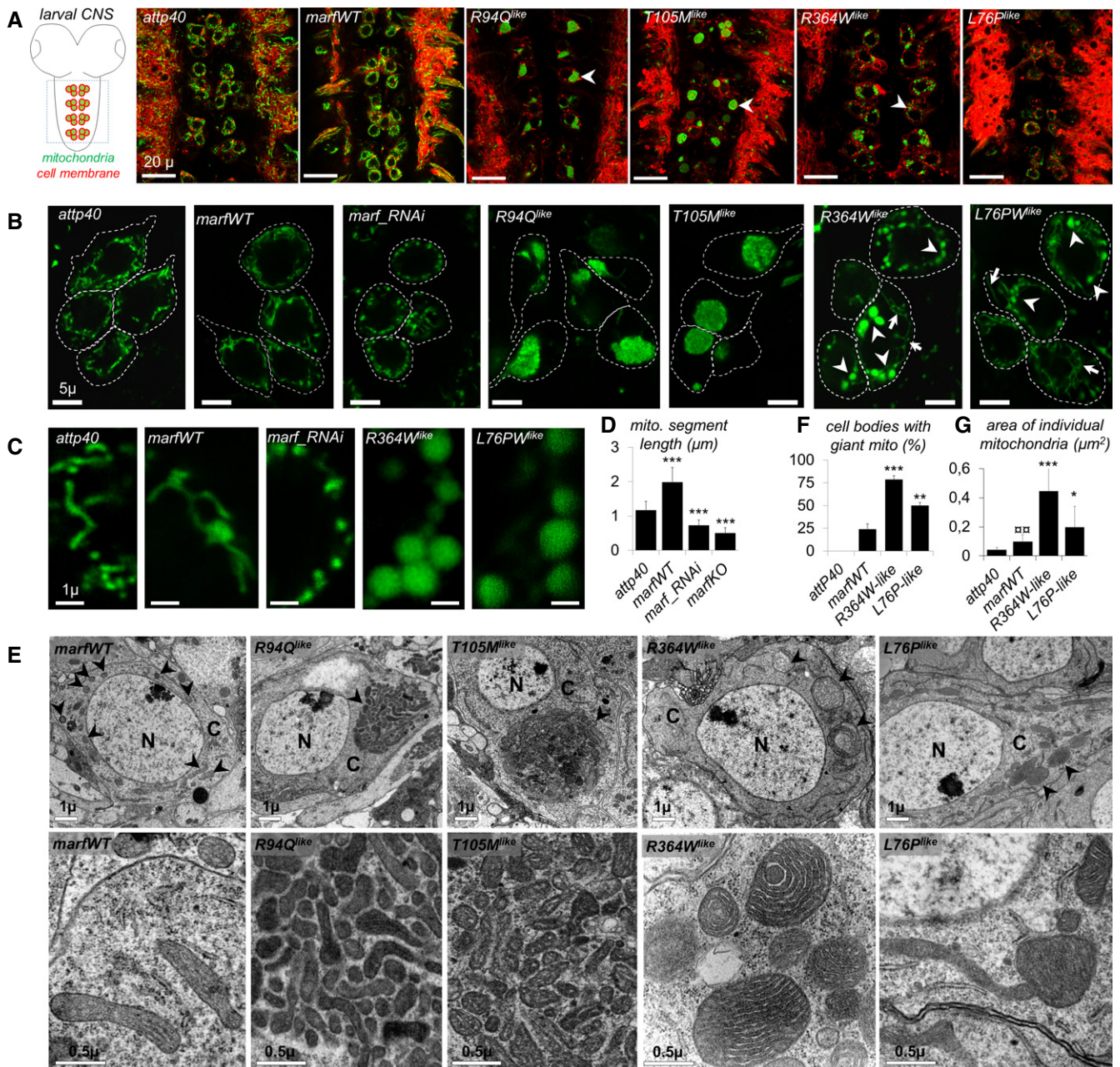


Figure 2. The CMT2A-mimetic alleles differently alter mitochondrial morphology in fly neurons.

A Scheme and confocal imaging of living larval ventral nerve cord showing midline motor neurons targeted by the *OK371-GAL4* driver (red: plasma membrane/myr::RFP; green: mitochondria/mit::dendra2). Arrowheads point to cell bodies with abnormal mitochondrial distribution/shape. Scale bars 20 μ m.

B Higher magnification views of living motor neuron cell bodies showing mitochondrial morphology (green: mitochondria/mit::dendra2). To facilitate mitochondrial observation, myr::RFP staining was used to draw the outline of the cell (dotted lines). *R364W^{like}* or *L76P^{like}*, arrowheads point to enlarged spherical mitochondria and arrows to mitochondrial tubules. See also: motor neuron-specific staining in Appendix Fig S1 and similar mitochondrial alterations induced upon pan-neuronal expression of the CMT2A alleles with the *elav-GAL4* driver Fig EV2. Scale bars 5 μ m.

C Higher magnification views of mitochondria (green: mitochondria/mit::dendra2; living tissue). Scale bars 1 μ m.

D Quantification of mitochondrial segment length (μ m) (number of mitochondria analyzed: *attp40*/212, *marfWT*/124, *marf_RNAi*/95, *marf^{KO}*/79). \pm SEM. Mann–Whitney *U* test results (versus *attp40*): ****P* < 0.001.

E Transmission electron microscopy sections of ventral nerve cord from larvae expressing the different *marf* alleles. Top panels: neuron cell body section showing cytoplasmic compartments (scale bars 1 μ m). Arrowheads point to mitochondria. N, nucleus; C, cytoplasm. Bottom panels: higher magnification views (scale bars 0.5 μ m).

F Average number of cell bodies containing giant spherical mitochondria (number of neurons analyzed: *attp40*/80, *marfWT*/72, *R364W^{like}*/96, *L76P^{like}*/118; four independent larval brains). \pm SEM. Mann–Whitney *U* test results (versus *marfWT*): ****P* < 0.001, ***P* < 0.01.

G Area quantification of individual mitochondria (μ m²). Number of mitochondria analyzed on EM sections: *attp40*/101, *marfWT*/118, *R364W^{like}*/190. \pm SEM. Mann–Whitney *U* test results: *R364W^{like}* or *L76P^{like}* versus *marfWT* ****P* < 0.001 and **P* < 0.05; *marfWT* versus *attp40* $\square\square$ *P* < 0.01.

(Fig 2E) that were on average bigger (Fig 2G). Cristae and matrix were electron dense and not distended (Fig 2E), demonstrating that increased size was not a consequence of unspecific swelling. To test whether the CMT2A alleles affect mitochondrial fusion, we performed *in vivo* photoconversion experiments. In control *marf*^{WT} neurons (Movie EV1 and detailed description of the experiment Fig EV3), mitochondrial tubules are fused and therefore photoconverted molecules of matrix-targeted Dendra2 (mit::dendra2) diffuse outside the initial photoconversion area. In contrast, red mit::dendra2 molecules remained in the vicinity of the photoconverted area in neurons expressing *R94Q^{like}* and *T105M^{like}*, showing that aggregated mitochondria are separate and cannot fuse in these cells (Movies EV2 and EV3, and Fig EV3). This was not the case in neurons expressing *R364W^{like}* and *L76P^{like}* in which the fluorescent probe was able to diffuse (Movies EV4–EV6 and Fig EV3). Taken together, these results show that mutations associated with the GTPase domain (*R94Q^{like}* and *T105M^{like}*) cluster mitochondria and inhibit fusion, whereas those within HB1 domain (*R364W^{like}* and *L76P^{like}*) trigger the formation of enlarged mitochondria that are well connected to the mitochondrial network.

Highly prevalent *R364W* allele encodes a fusion-competent mitofusin

The morphology, interconnectivity, and ultrastructure of mega-mitochondria suggested that, in contrast to *R94Q* and *T105M* mutants, *R364W* and *L76P* alleles do not impair mitochondrial fusion. In order to reveal the intrinsic activity of the CMT2A mutant, we expressed these pathogenic proteins in cells devoid of endogenous MFN. To that purpose, we generated knockout flies carrying a deletion which abolishes endogenous *marf* expression (Appendix Fig S2 and Fig 1D). In these flies, mitochondrial fragmentation was rescued by our *marf*^{WT} transgene, but not by *R94Q^{like}* and *T105M^{like}* that still aggregated mitochondria (Fig 3A). In contrast, *R364W^{like}* and *L76P^{like}* could restore mitochondrial tubules formation but also generated few large mitochondrial spheres (Fig 3A). To confirm that human *R364W* and *L76P* alleles encode fusion-competent MFNs, we analyzed their function in mouse embryonic fibroblasts (MEFs) devoid of MFN1 and MFN2. In this well-established experimental system [31], mitochondria, that are initially fragmented, elongate to form tubules upon expression of a fusion-competent MFN. Consistently, expression of mouse *MFN2* (Fig EV4A and C), human *MFN2* (Fig 3B and C), and *Drosophila marf* (Fig EV4A and C) transgenes restored filamentous mitochondrial morphology, confirming the high conservation of fusion machineries between these species. Then, transfection with human *MFN2* containing CMT2A mutations revealed that cells expressing *R94Q* and *T105M* did not form filamentous mitochondria and contained clustered mitochondria in a higher proportion (Figs 3B and C, and EV4B and C), while those expressing *L76P* and *R364W* were able to elongate mitochondria into tubules (Figs 3B and C, and EV4B and C). Of note, we observed more cells with filamentous mitochondria and less with aggregates upon transfection with *R364W* (Fig 3C). To directly assess mitochondrial fusion capacity, we used a polyethylene glycol (PEG)-based cell fusion assay [32]. We generated MEF lines stably expressing human wild-type or mutant *MFN2* alleles as well as red or green

fluorescent proteins targeted to mitochondria. After plasma membrane fusion of cells with green and red-labeled mitochondria, we quantified fusion-mediated exchange of mitochondrial fluorescent proteins. Consistently, whereas non-fusogenic mitochondria lacking mitofusins remained singly labeled (–/–, Fig 3D and E), those in which wild-type human *MFN2* was expressed appeared double-stained (*Hs-MFN2*, Fig 3D and E). In contrast, we confirmed that *MFN2-R94Q* is not fusion-competent (Fig 3D and E) and that the effect of this mutation is dominant, as mitochondria expressing this allele were unable to fuse with mitochondria expressing wild-type human *MFN2* (Figs 3F and EV4D). Most importantly, these fusion assays revealed that mitochondria expressing human *MFN2-R364W* display a fusion capacity that was similar (homotypic experiments, Fig 3D and E) or slightly higher (heterotypic experiments, Figs 3F and EV4D) to that of wild-type human *MFN2*. Taken together, these results confirm that *R94Q* and *T105M* mutants cannot support fusion but can still tether mitochondria and, surprisingly, demonstrate that *R364W* and *L76P* mutants are fusion-competent.

Enhanced mitochondrial fusion in *R364W* fly model

To understand how fusion-competent mutants can alter mitochondrial morphology in neurons and trigger neurological defects, we returned to the fly model. In the following analysis, we focused our study on the comparison between *R364W^{like}* and *R94Q^{like}* that mimic the two most frequent CMT2A alleles. We observed that neurons over-expressing *marf* via a previously described transgene [33], achieving higher *marf* expression level than our own *UAS-marf*^{WT} transgene (*marf*^{WT^{strong}}, Fig 1D), exhibited giant mitochondrial spheres (*marf*^{WT^{strong}}, Fig 4A) similar to those of *R364W^{like}*-expressing neurons. We thus inferred that giant mitochondria might originate from excessive mitochondrial fusion and a shift of the fusion/fission balance toward fusion. To test this hypothesis, we investigated whether the giant mitochondrial phenotype was similarly induced by decreasing mitochondrial fission. We showed that expression of a dominant negative mutant of the fission effector DRP1 (*drp1^{K38A}*) [34,35] also induced the formation of mitochondrial spheres similar to those found in *R364W* fly model (Fig 4A). In cells expressing *drp1^{K38A}*, knocking down *marf* restored normal mitochondrial morphology demonstrating that the giant mitochondrial phenotype was indeed a consequence of unbalanced mitochondrial fusion (Fig 4A). In order to shift the fusion/fission balance toward fission, we over-expressed *drp1* in the neurons of flies expressing the *R364W^{like}* allele. Consistent with our hypothesis, the giant mitochondria phenotype disappeared (Fig 4B and C), and the average mitochondrial size was close to that of controls (Fig 4D and E). Knocking down the inner-membrane fusion effector *opa1*, which is also expected to shift the fusion/fission balance toward fission, similarly led to a reduction of giant mitochondria in the *R364W^{like}* context (Fig 4B). We then performed the converse experiment by inhibiting fission in the *R364W* fly model and showed that neurons now contained one or few gigantic spherical mitochondria (Fig 4B and D) as a result of increased size (Fig 4E). In contrast, manipulating *drp1* or *opa1* activities did not interfere with the formation of mitochondrial aggregates in *R94Q* fly model (Fig 4B). Finally, we showed that over-expressing DRP1 was sufficient to normalize the locomotor performances in *L76P* and *R364W* fly models (Fig 1E, “+ *drp1*”) demonstrating that the excessive fusion

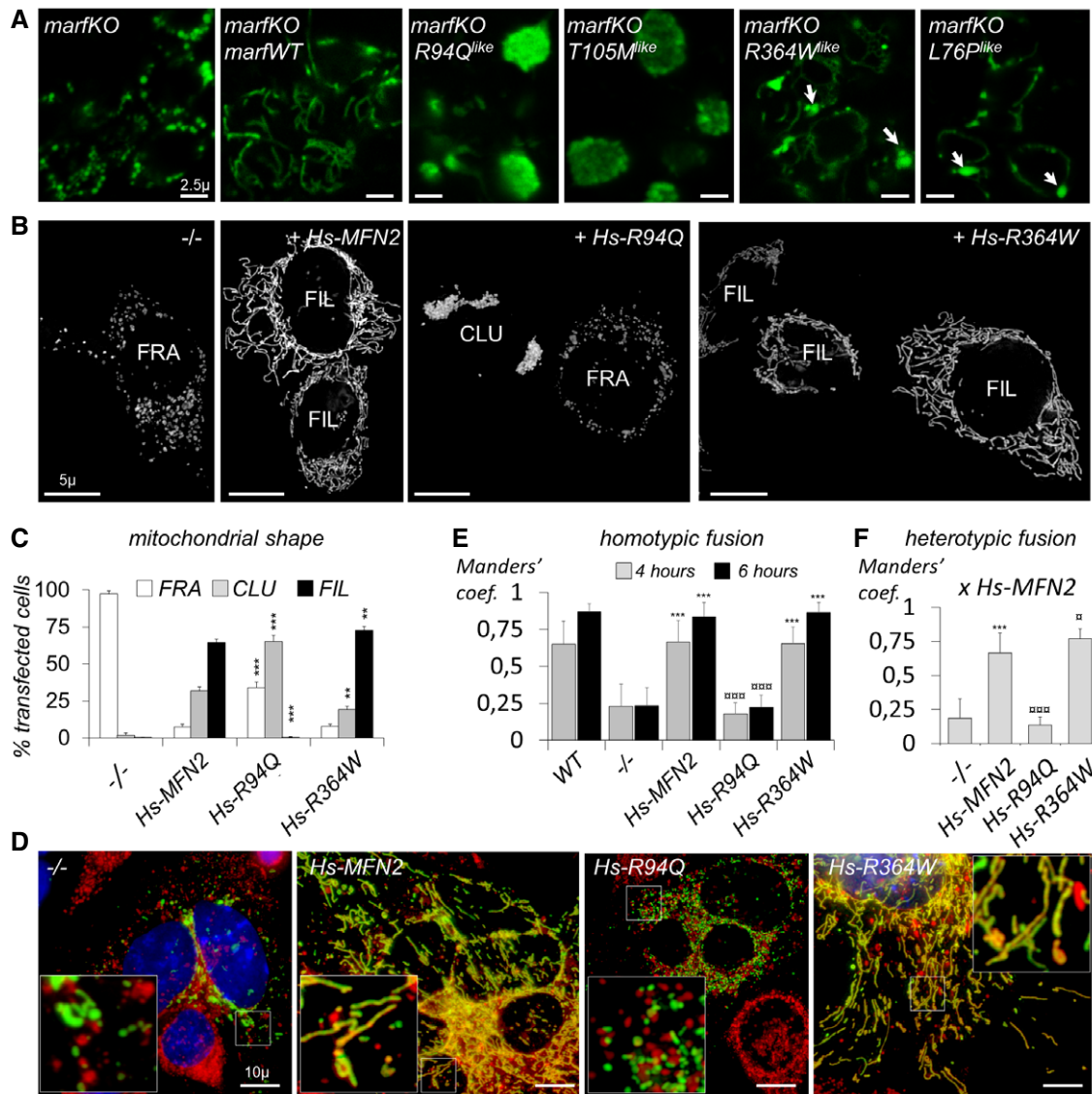


Figure 3. Pathogenic CMT2A alleles located to the helix bundle 1 (R364W, L76P) are fusion-competent in MFN-null fly neurons and mouse fibroblasts.

- A** Expression of the *marf* CMT2A alleles in motor neurons of *marf* knockout larvae (*marf*^{KO}/Y; *OK371-GAL4*, *UAS-mit::dendra2*). Arrows show mitochondrial spheres (living tissue). Although expression of *marf* wild-type or CMT2A transgenes in motor neurons rescues or modifies mitochondrial morphology, it does not rescue developmental delay and lethality of *marf* knockout larvae due to the lack of *marf* in whole body (see Appendix Fig S2 and methods for additional details regarding *marf* knockout animals). Scale bars 2.5 μ m.
- B** Mouse embryonic fibroblasts devoid of MFN1 and MFN2 (MFN1/MFN2-null cells) were transfected with mtGFP (GFP targeted to the mitochondrial matrix) alone (*-/-*) or co-transfected with wild-type human (Hs) MFN2 or with the *R94Q* or *R364W* mutants. Visualization of mitochondrial morphology by fluorescence microscopy of mtGFP. Bar: 5 μ m. Cells display fragmented (FRA), filamentous (FIL), and/or clustered (CLU) mitochondrial compartments. (see Fig EV4 for *T105M* and *L76P* and rescue with wild type mouse *MFN2* or *Drosophila marf*). Scale bars 5 μ m.
- C** Percentage of transfected mtGFP-positive cells displaying fragmented (FRA), filamentous (FIL), and/or clustered (CLU) mitochondrial morphology (mean \pm SD). Number of transfections = 5 (no MFN), 10 (*Hs-MFN2*), 6 (*R94Q*), 7 (*R364W*). Mann–Whitney *U* test results (versus *Hs-MFN2*): ***P* < 0.01, ****P* < 0.001.
- D** Polykaryons obtained by PEG-induced plasma membrane fusion of MEFs expressing GFP targeted to the matrix (mtGFP) or mCherry targeted to the outer membrane (mChOM). Images were taken 6 h after PEG-induced fusion. Fused mitochondria exchange red and green fluorescent proteins and appear doubly labeled. Unfused mitochondria remain singly labeled. DAPI-labeled nuclei appear in blue. Pictures show MFN1/MFN2-null MEFs (*-/-*) or MFN1/MFN2-null MEFs expressing wild-type (*Hs-MFN2*) or mutant human MFN2 alleles (*Hs-R94Q* and *Hs-R364W*). Scale bars 10 μ m.
- E** Histograms show the mean \pm SD of the Manders' colocalization coefficient for mtGFP in homotypic fusion assay as shown in (C). WT (wild-type MEFs), *-/-* (MFN1/MFN2-null MEFs), *Hs-MFN2* (*-/-* transduced with human wild-type MFN2), *Hs-R94Q*, and *Hs-R364W* (*-/-* transduced with corresponding human MFN2 alleles). Results are shown 4 or 6 h after PEG-induced fusion. Polykaryons analyzed (4 h/6 h): WT (15/15), *-/-* (15/15), *Hs-MFN2* (25/15), *Hs-R94Q* (15/15), *Hs-R364W* (25/15). Mann–Whitney *U* test results (* versus *-/-* 4 or 6 h, \square versus *Hs-MFN2* 4 or 6 h): ****P* < 0.001, \square *P* < 0.001.
- F** Histograms show the mean \pm SD of the Manders' colocalization coefficient for mtGFP in heterotypic experiments (PEG-induced fusion of MFN *-/-* MEFs expressing *Hs-MFN2*, labeled with mtGFP, with MFN *-/-* MEFs expressing *Hs-R94Q* or *Hs-R364W*, labeled with mCherryOM). Images are shown in Fig EV4D and were taken 4 h after PEG-induced fusion. Mann–Whitney *U* test results (* versus *-/-*, \square versus *Hs-MFN2*): ****P* < 0.001, \square *P* < 0.001, \square *P* < 0.05. Polykaryons analyzed: *-/-* (15), *Hs-MFN2* (25), *Hs-R94Q* (15), *Hs-R364W* (15).

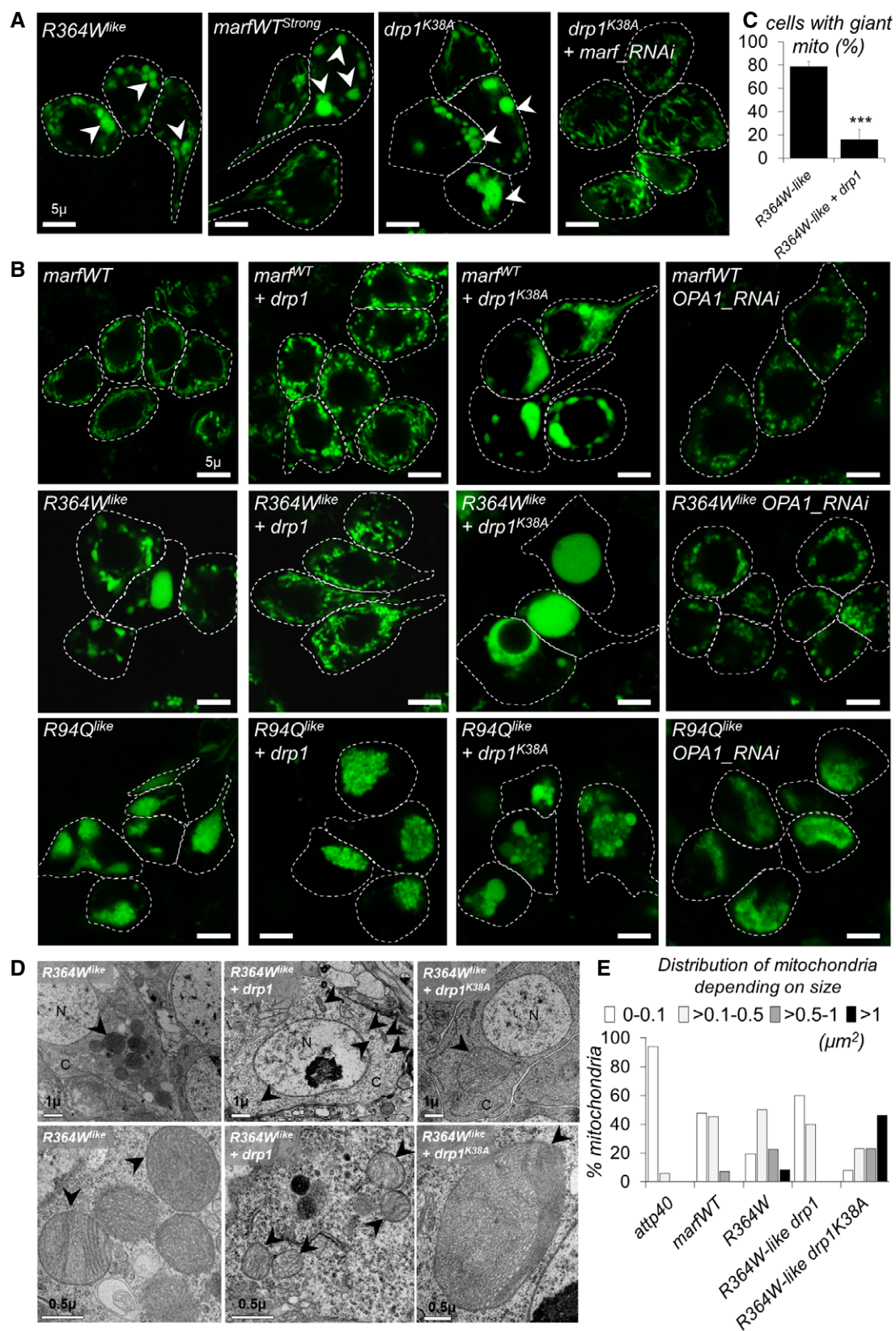


Figure 4.

Figure 4. Enhanced mitochondrial fusion in neurons of the R364W fly model.

- A Confocal images of mitochondria showing the presence of large mitochondrial spheres (arrowheads) in living larval motor neurons (*OK371-GAL4; UAS-mit::dendra2*) expressing the *marf*^{WTStrong} transgene (*marf* over-expression at higher expression level than our *UAS-marf*^{WT} transgene), or *drp1*^{K38A} + *marf*^{RNAi} (RNAi against *marf*). White line: plasma membrane according to myr::RFP staining. Scale bars 5 μ m.
- B Confocal images of mitochondria (*mit::dendra2*) in living larval motor neurons expressing *marf*^{WT}, *R364W*^{like}, *R94Q*^{like} in conjunction with various UAS transgene. + *drp1*: over-expression of the fission effector DRP1; + *drp1*^{K38A} over-expression of dominant negative DRP1; and + *OPA1*^{RNAi}: RNAi downregulation of the fusion factor OPA1. White line: plasma membrane according to myr::RFP staining. Scale bars 5 μ m.
- C Quantification of the number of cells containing giant spherical mitochondria \pm SEM. Number of cells analyzed: *R364W*^{like}/96, *R364W*^{like} + *drp1*/70. Mann–Whitney *U* test results: *R364W*^{like} versus *R364W*^{like} + *drp1* ****P* < 0.01.
- D TEM images of neurons from larval ventral nerve cords. Top panels: cell bodies (arrowheads, mitochondria; N, nucleus; C, cytoplasm); scale bars 1 μ m. Bottom panels: higher magnification images highlighting mitochondrial morphology; scale bars 0.5 μ m. + *drp1*: over-expression of *drp1* and + *drp1*^{K38A}: dominant negative DRP1.
- E Size distribution of individual mitochondria (area μ m²). Number of mitochondria analyzed: *atp40*/101, *marf*^{WT}/118, *R364W*^{like}/190, *R364W*^{like} + *drp1*/108, *R364W*^{like} + *drp1*^{K38A}/44. Mann–Whitney *U* test results performed on the average value of the area: *atp40* versus *marf*^{WT} *P* < 0.05; *marf*^{WT} versus *R364W*^{like} *P* < 0.001, *R364W*^{like} versus *R364W*^{like} + *drp1* *P* < 0.001, *R364W*^{like} versus *R364W*^{like} + *drp1*^{K38A} *P* < 0.01.

of mitochondria in neurons is the primary pathogenic mechanism of these alleles.

Increased mitochondrial damages in neurons of R94Q and R364W fly models

While analyzing mitochondrial morphology by electron microscopy, we noticed that neurons expressing *R364W*^{like} and *R94Q*^{like} contained vesicular structures (Fig 5A) that were never observed in *marf*^{WT} control animals. These structures were found very close to mitochondria and, at the ultrastructural level, appear as multi-lamellar structures evocating autophagy figures (Fig 5A, arrowheads) that sometimes contacted or contained mitochondria (Fig 5A, arrows). In *Drosophila*, increased transcription of autophagy genes (*atg*) accompanied the autophagic process in various contexts [36,37]. By quantifying the expression level of *atg8b*, the fly homolog of the canonical autophagy marker LC3, we revealed an up-regulation of this gene in *R364W*^{like} and *R94Q*^{like} fly brains (Fig 5B). Together with the presence of multi-lamellar structures, this qPCR result suggested that autophagy is activated in the brains of *R364W* and *R94Q* fly models. As autophagy is known to be involved in the degradation of damaged mitochondria, we speculate that increased autophagy in CMT2A-mimetic flies could represent a cellular response to the accumulation of damaged

mitochondria. Because a hallmark of mitochondrial damages is the alterations of oxidative metabolism, we quantified ATP levels in CMT2A fly brains extracts using a luciferase-based assay and observed decreased ATP levels in both *R364W*^{like} and *R94Q*^{like} animals (Fig 5C). Another consequence of altered oxidative metabolism is the accumulation of ROS that can be released from defective mitochondrial respiratory chains. Of note, ROS, which trigger oxidative stress, are also known inducers of autophagy. To test whether ROS accumulate in CMT2A neurons, we stained fly brains with the fluorescent *in situ* probe DHE. Quantifications revealed higher level of fluorescence in *R364W*^{like} and *R94Q*^{like} brains compared to control *marf*^{WT} (Fig 5D). To test more directly the hypothesis that damaged mitochondria accumulate in CMT2A flies, we quantified the level of mtDNA mutations which accumulate during the life of most animals including flies [38]. Having first shown that the CMT2A-mimetic flies have normal mtDNA level (Fig 5E), we then measured mtDNA mutation load using a random mutation capture assay (RMC). Consistent with our hypothesis, this qRT–PCR analysis revealed that brains from *R364W* and *R94Q* fly models accumulate more mutant mtDNA molecules than controls during their development (Fig 5F). Finally, we showed that, in *R364W*-mimetic flies, over-expressing *drp1* was sufficient to decrease mtDNA mutation load, *atg8b* expression, and ROS level, and to increase ATP (Fig 5B–D and F), confirming that

Figure 5. The CMT2A alleles compromise mitochondrial integrity and function.

- A Transmission electron microscopy images from larval ventral nerve cord expressing *R364W*^{like} and *R94Q*^{like}. Arrowheads show multi-lamellar vesicular structures in the vicinity of mitochondria evocating autophagy figures. These structures sometimes contained mitochondria (arrows). Scale bars 0.2 μ m.
- B qRT–PCR on third-instar larvae central nervous system showing *atg8b* mRNA level \pm SEM relative to control (*elav>marf*^{WT}). Mean value obtained for four independent mRNA extracts each from 12 dissected brains. Mann–Whitney *U* test results: *marf*^{WT} versus *R364W*^{like} or *R94Q*^{like} ****P* < 0.001; *R364W*^{like} versus *R364W*^{like} + *drp1* \square *P* < 0.001.
- C Average ATP level in third-instar larval brains (% of control level) \pm SEM. Three independent experiments performed on extracts from five *elav-GAL4* adult fly brains. Mann–Whitney *U* test results: *marf*^{WT} versus *R364W*^{like}, *R94Q*^{like} ****P* < 0.01; *R364W*^{like} versus *R94Q*^{like} #*P* < 0.05, *R364W*^{like} versus *R364W*^{like} + *drp1* \square *P* < 0.05.
- D Images show DHE staining in neuron cell bodies from larval ventral nerve cord (scale bars 5 μ m). Quantification of ROS labeling intensity \pm SEM (ImageJ). Number of cell bodies analyzed *marf*^{WT}/194, *R94Q*^{like}/93, *R364W*^{like}/162, *R364W*^{like} + *drp1*/221 (from 10 to 12 larval brains). Mann–Whitney *U* test results: *marf*^{WT} versus *R364W*^{like}, *R94Q*^{like} ****P* < 0.01, ****P* < 0.001; *R364W*^{like} versus *R364W*^{like} + *drp1* \square *P* < 0.001.
- E Relative mtDNA levels measured by quantitative real-time PCR \pm SEM. Normalization is based on the amplification of nuclear *rp49* gene. Three independent qRT–PCR experiments each done on DNA extracts from 12 *elav-GAL4* dissected adult fly brains (3-day-old flies). No statistically significant difference.
- F Relative mitochondrial DNA (mtDNA) mutation load determined by RMC in extracts from *elav-GAL4 UAS-marf* (WT, *R94Q*^{like}, and *R364W*^{like}) dissected third-instar larval CNS and adult brains (3-day-old flies). \pm SEM. After extraction, DNA is digested by *TaqI* restriction enzyme and submitted to PCR. Primers flanking a *TaqI* site are used to amplify only mtDNA fragments in which the *TaqI* site sequence has been mutated. The amount of mutated DNA is normalized to total mtDNA level (determined by qRT–PCR using primers which do not flank a *TaqI* site). Eight independent experiments for *marf*^{WT}, seven for *R364W*^{like}, three for *R364W*^{like} + *drp1*, and three for *R94Q*^{like}. DNA extracts were prepared from 12 dissected larval CNS or adult brains. Mann–Whitney *U* test results: *marf*^{WT} versus *R364W*^{like}, *R94Q*^{like} ****P* < 0.001, ***P* < 0.01; *R364W*^{like} versus *R364W*^{like} + *drp1* \square *P* < 0.001, \square < 0.05.

excess of fusion is the most probable cause for neuronal dysfunction in the *R364W* fly model. Based on these observations, it is tempting to speculate that the pro-fusion activity of *R364W^{like}*, and the pro-aggregative activity of *R94Q^{like}*, leads to the accumulation of mitochondrial damages, reducing ATP and increasing ROS levels. Mitochondrial dysfunction can lead to neurodegeneration. However, as described for CMT2A patients, we did not observed motor neuron loss in our fly models (Fig EV5A and B). Nevertheless, a moderate degeneration was detected in the visual system (Fig EV5C and D), a situation evocating CMT6 disease.

levels. Mitochondrial dysfunction can lead to neurodegeneration. However, as described for CMT2A patients, we did not observed motor neuron loss in our fly models (Fig EV5A and B). Nevertheless, a moderate degeneration was detected in the visual system (Fig EV5C and D), a situation evocating CMT6 disease.

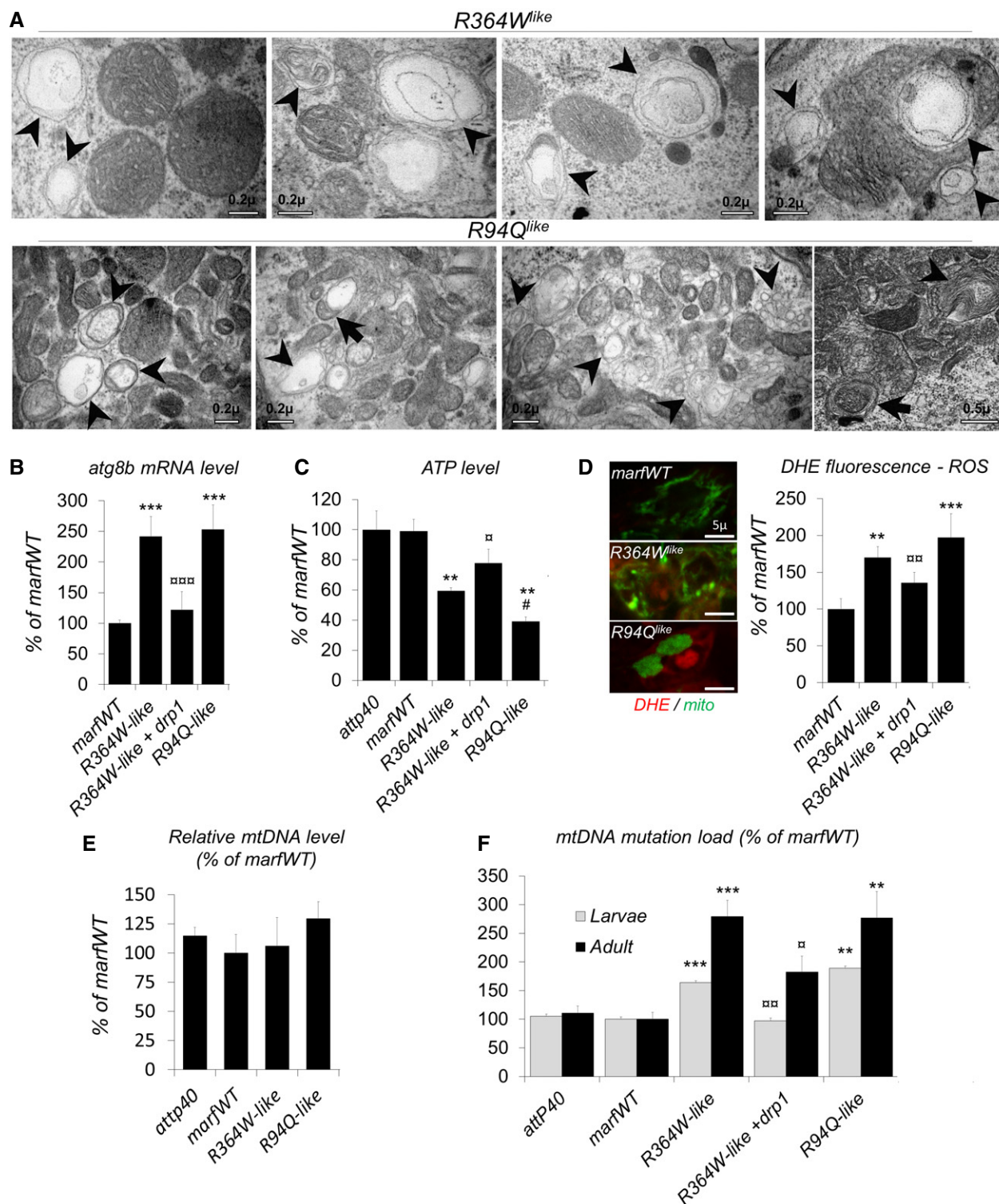


Figure 5.

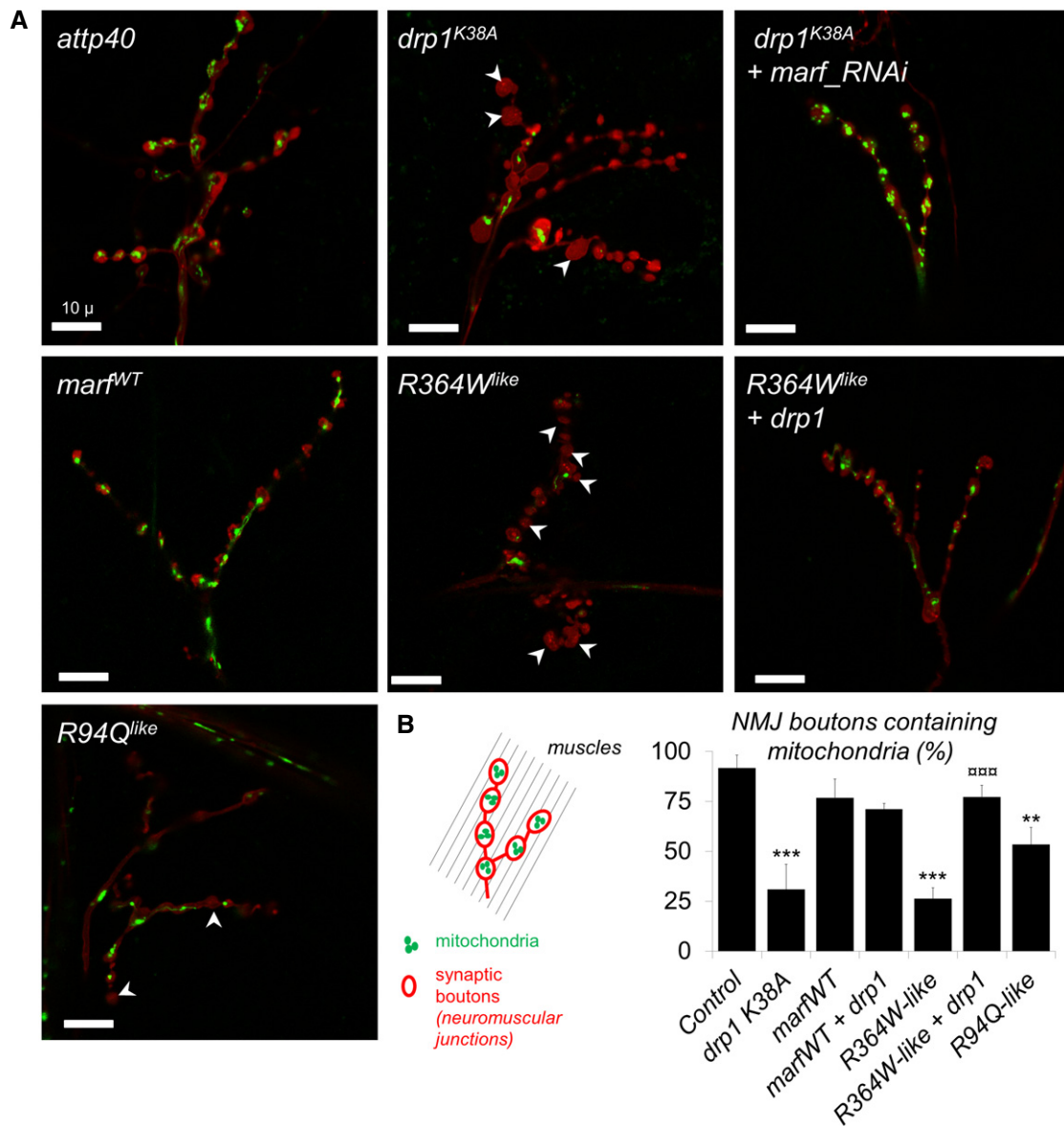


Figure 6. The CMT2A alleles trigger mitochondrial depletion at neuromuscular junctions.

A Confocal images of larval neuromuscular junctions (NMJ) targeted by *OK371-GAL4*. Synaptic bouton membrane is stained in red (myr::RFP) and mitochondria in green (mit::dendra2). Arrowheads: boutons without mitochondria. Scale bars 10 μ m.

B Proportion of synaptic boutons with mitochondria staining \pm SEM. Number of boutons analyzed: *attp40*/158, *drp1^{K38A}*/156, *drp1^{K38A} marf^{RNAi}*/172, *marf^{WT}*/216, *R94Q^{like}*/200, *R364W^{like}*/129, *R364W^{like} + drp1*/128. Mann–Whitney *U* test results: ****P* < 0.001, ***P* < 0.01 (versus *marf^{WT}*), □□□*P* < 0.001 (versus *R364W^{like}*).

Mitochondrial depletion at the neuromuscular junctions of *R94Q* and *R364W* fly models

We then asked whether the mitochondrial alterations in the neuronal soma could affect the localization of mitochondria at the neuromuscular junctions (NMJs) of the CMT2A flies. Indeed, the inactivation of *drp1*, which triggers the hyperfusion of mitochondria in neuronal soma, was shown to cause a dramatic depletion of mitochondria at NMJs [22]. To visualize mitochondria at NMJs *in vivo*, we expressed two fluorescent reporter proteins in motor neurons, the one labeling mitochondria in green and the other the plasma

membranes in red to allow the visualization of synaptic boutons at the muscle surface (Fig 6). First, we confirmed that, contrary to control NMJs, those of motor neurons in which *drp1* was inactivated were largely devoid of mitochondria (Fig 6A and B). We also demonstrated that this phenotype was rescued by *marf* knockdown (Fig 6A and B) showing that the localization of mitochondria at NMJs depends on a precise balance between mitochondrial fusion and fission. This analysis further revealed that the fraction of boutons devoid of mitochondria is significantly higher at the NMJs of *R364W^{like}*-expressing larvae (Fig 6A) and that over-expressing wild-type *drp1* restored mitochondrial distribution in boutons

(Fig 6A and B). Finally, we observed that mitochondrial aggregation in the neuron expressing *R94Q^{like}* was also associated with synaptic mitochondrial depletion. The degree of mitochondrial depletion was, however, lower than that observed in *R364W^{like}* animals (Fig 6A and B). These results demonstrate that shifts in the fusion/fission equilibrium interfere with mitochondrial localization at NMJs and, notably, that excess mitochondrial fusion provokes mitochondrial depletion at NMJs in the *R364W* fly model.

Discussion

In this work, we have generated and characterized *Drosophila* models of CMT2A-expressing pathogenic alleles in a wild-type background and at levels similar to that of endogenous MFN, a situation which resembles that of neurons carrying *MFN2* dominant heterozygous mutations. Our *in vivo* analysis of four CMT2A mutations, including the two most frequent alleles (*R94Q* and *R364W*), demonstrates that CMT2A mutations can induce aberrant mitochondrial morphology and function, mitochondria depletion at NMJ, and locomotor deficits by either deficient or excessive MFN activity.

Because mutations of the MFN2-GTPase domain, which are the most prevalent among CMT2A, have lost their ability to drive fusion in MEFs devoid of endogenous MFN (Fig 3 and [31]) and are genetically dominant in human patients and mouse models [26–28], they were proposed to encode dominant negative forms of MFN2 that decrease mitochondrial fusion and thereby induce neuronal dysfunction. However, there was so far no experimental evidence supporting this hypothesis in *in vivo* neurons. Our study reveals that mutations homologous to *R94Q* and *T105M* do not simply result in mitochondrial fragmentation (as observed in *marf* knockout flies), but rather trigger a massive aggregation of unfused mitochondria in fly neurons. Importantly, in our models, mutant and wild-type *marf* transgenes are expressed at similar levels that are near the endogenous *marf* level and, in this condition, control *marf^{WT}* transgene does not trigger mitochondrial clustering. Therefore, our data strongly support the idea that mitochondrial aggregation results from specific properties of the mutant alleles and not from unspecific effect of MFN over-expression as observed in cultured cells ([39,40], discussed in [27,41]). Of note, and consistent with this hypothesis, focal mitochondrial aggregates have been reported in the few available electron microscopy analysis of nerve biopsies from CMT2A patients [3,42,43]. At the molecular level, we can speculate that *R94Q* and *T105M* mutant MFNs retain the capacity to tether mitochondria, but cannot support the subsequent GTP-dependent steps that normally drive membrane fusion, as suggested by the poor diffusion of the probe in photoconversion experiments. Consequently, the defective MFNs might remain locked together, leading to progressive aggregation of a growing number of mitochondria. We thus propose that *R94Q* and *T105M* act as dominant negative MFNs that impair mitochondrial fusion and favor clustering.

Unexpectedly, our characterization of the *R364W* and *L76P* alleles reveals for the first time that two alleles known to cause CMT2A, including the highly prevalent *R364W* substitution, stimulate mitochondrial fusion activity and subsequently exert their toxicity by shifting the fission/fusion balance toward fusion. Indeed, we here show that, in fly neurons, mutations in residues homologous to

R364W and *L76P* result in the formation of large mitochondrial spheres similar to those induced by inactivating *drp1* or over-expressing at high-level wild-type *marf*. Such phenomenon is not a specificity of fly neurons, as enlarged globular mitochondria, strikingly similar to those described here in *Drosophila*, were also observed in the neuronal cell bodies of *drp1* knockout mice [21,44,45]. Interestingly, the latter studies have also shown that these giant mitochondrial spheres observed in neurons *in vivo* are absent from cultured *drp1* knockout MEFs [44,45] as showed here in MEFs expressing *R364W* and *L76P*. Consistent with the neuronal specificity of CMT2A, the analysis of skin fibroblast derived from CMT2A patients shows minor alterations of mitochondrial morphology and function [46–48]. This implies (i) that the formation of giant mitochondrial spheres may require factors or cellular properties that are specific of neurons, and (ii) that the validation of this pathogenic mechanism in mammals demands functional characterization of the *R364W* allele in neurons and not in fibroblasts.

The precise mechanism by which MFNs drive outer membrane fusion remaining debated, we can only speculate on the mechanisms by which *R364W* and *L76P* mutations might provoke MFN gain of function. As neither residue localizes to the GTP-binding domain or to any of the predicted coiled-coil domains (Figs 1A and EV1), it appears uncertain that they play a direct role in GTP-binding and hydrolysis, GTP-dependent MFN dimerization [49,50], and/or inter-mitochondrial tethering via coiled-coil domains [51,52]. In the MFN1 structure, the homologs of L76 and R364 (V55 and R343) localize to the helix bundle HB1 (Fig EV1B and C) that is homologous to the neck domain of the bacterial dynamin BDLP (Fig EV1C and D). Of note, a transition between condensed and extended conformations (Fig EV1D and E) has been proposed to underlie the function of BDLP [53] and of the related MFNs [14]. In the condensed conformation, these residues (Fig EV1C and D: blue) would be oriented toward the predicted second helix bundle HB2, homologous to the trunk domain of BDLP (Fig EV1C and D: yellow) and in close proximity of an interbundle domain of highly variable structure located between both helix bundles (Fig EV1C and D: green). It is therefore tempting to propose that these residues participate in HB1/HB2 (Neck/Trunk) interactions and somehow contribute to the stability of the condensed conformation and/or to modulating the shifts between the condensed and extended forms (Fig EV1D and E).

Our microscopy data demonstrate that both mitochondrial aggregation and excessive fusion are associated with a depletion of mitochondria at NMJs in our CMT2A fly models. In the *R94Q* fly model, this phenotype might reflect the fact that “sticky” mitochondria trapped within aggregates observed in neuronal cell bodies are not free to move in thin axonal projection to reach synapses. In the *R364W* fly model, this is rather the shift of the fusion/fission balance in favor of fusion that is responsible for mitochondrial loss in NMJs. In flies and mammals, a similar depletion of synaptic mitochondria is indeed observed when fission is inhibited (this manuscript and [22,54]). Fission seems therefore required for the efficient transport of mitochondria to synapses possibly because this process maintains mitochondrial size down to a level compatible with mitochondrial movement into neuronal projections or with the interaction of mitochondria with the transport machinery. Mitochondrial depletion at NMJs may impair neurotransmission in CMT2A flies as previously described in flies

mutant for DRP1 or for the mitochondrial kinesin adaptor Milton [22,55]. Indeed, in fly, as well as in mammalian neurons, synaptic mitochondria provide the ATP required by the synaptic machinery [22,56] and tune down calcium waves in axon terminals [57,58]. There is so far no available histological study of nerve biopsies from patients with mutations of the R364 residue. However, if *R364W* affects mitochondrial distribution at the NMJs in human as it does in flies, it would presumably impact neuronal activity. It is indeed known that mutations affecting proteins involved in mitochondrial axonal transport, such as dyneins DYNC1H1 and DNAH10, and dynactin DCTN2, are sufficient to cause axonal forms of CMT [59,60].

Additionally, increased mtDNA mutation load correlating with autophagy markers up-regulation, decreased ATP, and increased ROS were detected in the brain of *R94Q* and *R364W*-mimetic flies. These observations suggest that damaged organelles accumulate in the neurons of these animals and may contribute to neuronal dysfunctions. In the *R364W* fly model, increasing fission resettled mtDNA mutation load, autophagy markers, ATP, and ROS toward normal level, suggesting that this CMT2A allele compromises the removal of defective mitochondria by switching the fission/fusion balance toward fusion. Accordingly, inhibiting fission was shown to decrease the efficacy of mitophagy, resulting in the accumulation of oxidized mitochondrial proteins and subsequently decreasing oxidative metabolism [21,61–63]. Indeed, fission is proposed to support the sorting of mitochondria depending on their metabolic activity, the poorly active being isolated and degraded [61]. Additional studies in yeast also revealed that the segregation of poorly active mitochondria relies on lower fusion capacity [64]. Therefore, by favoring mitochondrial fusion over fission, the *R364W* allele might compromise the elimination of defective mitochondria by decreasing the efficacy of the mitochondrial sorting process. In *R94Q* fly model, mitochondrial aggregation might also affect the elimination of damaged mitochondria possibly because mitochondria trapped into dense aggregates are poorly accessible to the vesicular components of the autophagy machinery. Similar pathogenic process might arise in human, as decreased oxidative metabolism was associated with increased level of deleted mtDNA molecules in fibroblasts from CMT2A patients [48]. However, aggregation is not the only deleterious consequence of *R94Q*. Indeed, this mutation impairs inter-mitochondrial exchanges suggesting that the *R94Q* allele acts as a dominant negative MFN which inhibits the mitochondrial fusion process. This would presumably compromise the buffering of mitochondrial damaged explaining why *R94Q* flies experience more severe neurological defects and have lower brain ATP levels than *R364W*-mimetic animals, despite higher mitochondrial synaptic density, and similar brain mtDNA mutation load.

In conclusion, we propose that CMT2A does not simply result from decreased MFN activity but rather from more complex alterations of MFN functions. Depending on the alleles, CMT2A mutations result in mitochondrial clustering or unexpectedly enhance mitochondrial fusion subsequently affecting mitochondrial distribution and integrity in neurons. Our data also indicate that anti-fission or pro-fusion drugs, envisioned as treatments for CMT2A or neurodegenerative disease [18,52,65], could be detrimental for patients with *R364W* and *L76P* alleles that would rather benefit from the development of pro-fission or anti-fusion molecules.

Materials and Methods

Sequence/structure analysis

Alignments of MFN1/NP_284941, MFN2/NP_001121132, MARF/NP_996358, and BDLP/B2IZD3 were performed with CLUSTALW or MUSCLE (<https://npsa-prabi.ibcp.fr> or www.phylogeny.fr). Coiled-coil and transmembrane domains were predicted with COILS and TMPred software (<http://www.ch.embnet.org>) [40]. 3D structures of MFN1-MGD ([49]; PDB ID 5GNU, 5GNT), MFN1_{IM} ([50]; PDB ID 5GO4, 5GOE), and BDLP ([66]; PDB ID 2J68, 2J69, 2W6D) were retrieved from RCSB Protein Bank (www.rcsb.org). Structural alignments were performed with TM-align [67].

Mitochondrial morphology and fusion in mammalian cells

We used mouse embryonic fibroblasts (MEFs) with a wild-type genotype [16] or devoid of MFN1 and MFN2 (MFN1/MFN2-null cells [51]). For transient expression, MEFs were co-transfected using Turbofect (Thermo Fisher) with pCB6-mtGFP [40] and pQCXIB (Addgene plasmid # 22800) plasmids encoding mouse MFN2, *Drosophila* MARF, human MFN2, or indicated human MFN2 mutants. For quantitative analysis, mitochondrial morphology of 100–150 transfected cells was determined and expressed as percentage transfected cells with fragmented/FRA, filamentous/FIL, or clustered/CLU mitochondria.

For stable transduction of MEFs, viral particles were generated by transfection of Plat-E retroviral packaging cells (Cell Biolabs, Inc.) with retroviral plasmids encoding GFP targeted to the mitochondrial matrix (pMXs-puro-mtGFP), mCherry anchored to the outer membrane by the transmembrane domain of OMP25 (pMXs-puro-mChOM [32]) or the indicated MFN2 alleles (pQCXIB-MFN2). MEFs were transduced with viral supernatants diluted in complete culture medium and supplemented with 8 µg/ml polybrene. Transduced cells were selected with 20 µg/ml blasticidin and/or 2 µg/ml puromycin. Expression of fluorescent proteins was confirmed by fluorescence microscopy. Expression of MFN2 alleles was confirmed by Western blot with MFN2-specific antibodies [40].

Mouse embryonic fibroblasts expressing either mtGFP or mCherryOM were co-plated on glass coverslips and subjected to cell fusion with P.E.G. as described [32]. Fused cells were maintained in cycloheximide containing medium (20 µg/ml) to inhibit protein synthesis and fixed after 4 or 6 h. MEFs were imaged with a 100× objective in an Olympus IX81 microscope. Z-stacks were deconvoluted using the DeconvolutionLab plugin [68] and combined into a Maximum Intensity Projection with ImageJ or the Extended Focus option of CellR software (Olympus). To quantify the colocalization between mtGFP and mChOM, we calculated the Manders' coefficients using the JaCOP plugin of ImageJ software [69]. Regions of high mitochondrial density (essentially perinuclear regions) were excluded from the analysis to avoid colocalization artifacts due to insufficient spatial resolution.

Drosophila stocks and culture

UAS-CMT2A lines

marf coding sequence was amplified from *w¹¹¹⁸* fly, cloned into pDonr221 vector and checked by sequencing. *marf* 5' and 3' UTRs

were not included, and only a kozak CAAA sequence was added in front of ATG. The R404W (*R364W^{like}*), L118P (*L76P^{like}*), R135Q (*R94Q^{like}*), and T146M (*T105M^{like}*) were made using quick change PCR (Agilent) that cloned (Gateway) into *pUAST-w⁺-attB*. Vectors carrying wild-type or mutant *marf* were inserted by phiC31-mediated transgenesis (injection into *white* flies carrying *attP40* insertion site).

UAS-mit::dendra2

A Gateway cassette was cloned into *pUASp-w⁺* in front of Dendra2 [70] coding sequence. This plasmid was used to fuse the mitochondrial target sequence of human COVIII (MSVLTPLLLRGLTGSARRLPV-PRAKIHSL) with Dendra2. Independent lines were obtained by P-Element transgenesis. The 4M line (2nd chromosome) was used here.

marf knockout flies

Homologous recombination was realized by ends-out targeting. The resulting deletion starts 10-bp upstream of ATG and up to stop codon. 5' and 3' homology regions (around 2.8 kb) were PCR amplified from *W¹¹¹⁸* flies and cloned in *PTV-cherry* at *KpnI* and *Ascl* sites (5'HR primers: 5'CATCACCTCGATGACTC and 5'GGTTTATGGTTGATTCG, 3'HR primers: 5'TAGTGGAACAGTAGTGGG and 5'ATGCGACTGGTGCTTGCA). To validate *W⁺ marf* knockout animals, the 5' and 3' boundary regions between the remaining sequences of the *marf* locus and the inserted *PTV-cherry* construct were sequenced. Heterozygous *marf^{KO}* adults are fully viable and fertile, but hemizygous male and homozygous female larvae show extended larval stage, growth defect, and third-instar lethality as described for the *marf^B* mutant alleles in [71].

Other lines

UAS-drp1 and *UAS-drp1^{K38A}* were from J. Chung, *UAS-marf^{Strong}*, *UAS-marf^{RNAi}*, and *UAS-OPA1^{RNAi}* from M. Guo, and *elav-GAL4*, *OK371-GAL4*, and *UAS-myr::RFP* from Bloomington stock center. *GAL4/UAS* fly crosses were grown at 29°C on cornmeal-agar diet.

Quantitative real-time PCR

mRNAs were extracted from 12 dissected third-instar larval brains, submitted to retrotranscription followed by qRT-PCR [SyBR GreenER Supermix/Life Technologies/PCR program: 7 min at 95°C, 41× (15 s at 95°C, 1 min at 60°C)]. The following primers were used: 5'TGTCGTTGATCTCAGCTTC/5'GGTAGATGCAGCCGTAGAGG (exonic region) to detect products transcribed from endogenous *marf*, and from *marf* UAS transgenes, and 5'GGGGCAAACACTAACCAGA/5'GTTGCAGCAAATACGTGGT to detect only products of endogenous *marf* (3' UTR region that is absent from the *marf* UAS transgenes). For *atg8b*, we used 5'GGGAGCCTTCTCGACGAT/5'TTCATTGCAATCATGAAGTTCC. The amount of mRNA detected was normalized to control *rp49* mRNA values (5'GACGCTTCAAGGGACAGTATCTG and 5'AAACGCGGTTCTGCATGA). Normalized data were used to determine the relative *marf* mRNA levels according to cycling threshold analysis.

In situ labeling

For *in situ* detection of *mit::dendra2* and *myr::RFP*, living larval central nervous systems were rapidly dissected, mounted into PBS, and immediately imaged. For even-skipped (Hybridoma Bank, 2B8)

immunolabeling, tissues were dissected in PBS, fixed for 5 min in 4% formaldehyde, washed 5 min, and saturated 1 h in 0.5% BSA, 0.1% Triton in PBS (PBTB). Primary anti-Eve diluted in PBTB was incubated ON at 4°C, and later washed 1 h in 0.1% Tween-20 in PBS (PBTw). Secondary antibody was incubated 2 h and washed 1 h in PBTw. Preparations were mounted in Vectashield/DAPI (Vector). A LSM780 Zeiss confocal microscope was used for imaging.

Time-lapse microscopy

OK-GAL4; UAS-mit::dendra2 third-instar larva central nervous systems were rapidly dissected and mounted in PBS. Observations were carried out under a *Roper-Nikon* spinning disk confocal microscope equipped with photoconversion module controlled by *Metamorph*. A 450 nm laser (10% power) was used to photoconvert *mit::dendra2* molecules (120 ms). Confocal images of green (laser excitation 488 nm) and red (laser excitation 545 nm) *mit::dendra2* signals were acquired repetitively during a time window of 120 s (duration of each red/green acquisitions 3 s).

Electron microscopy

Larval ventral nerve cords were dissected and immediately fixed in 2% paraformaldehyde, 2.5% glutaraldehyde, 5 mM CaCl₂, and 0.1 mM Na cacodylate for 24 h at 4°C. This was followed by 2 h post-fixation in 2.5% glutaraldehyde, 0.8% osmium tetroxide, and 0.1 mM Na cacodylate at 4°C. Ultrathin Epon plastic sections were examined with a Tecnai G2 TEM.

Locomotor performance

Fly locomotor performance was determined using negative geotaxis test. Ten flies were placed in a clean plastic column (25 cm tall × internal diameter 1.5 cm) and gently tapped to the bottom. After 30 s, the flies at the top of the column (*N_{top}*) and the flies remaining at the bottom (*N_{bot}*) were counted. Three trials were performed at 30-s intervals. The performance index was defined as $(1/2 * (10 + N_{top} - N_{bot})/10)$.

ATP level

ATP measurements were performed according to manufacturer's instructions (Luminescent ATP detection assay kit, Abcam). For each experiment, five adult fly brains were rapidly dissected, and the extracts were immediately deproteinized by perchloric acid precipitation. Luminescent was measured with a TriStar LB941 luminometer.

Superoxide staining

DHE staining was performed as described [72]. Third-instar larval central nervous systems were dissected in PBS and incubated 5 min in 30 μM DHE (in Schneider's medium) at room temperature, washed and fixed 8 min in 4% formaldehyde. DHE (excitation 350 nm, emission 430 nm) is oxidized by superoxide free radicals into ethidium (excitation 530 nm, emission 620 nm). The ethidium signal was detected with a LSM780 confocal microscope (Zeiss). Pixel density was determined using the ImageJ.

mtDNA quantification

Twelve adult fly brains (3-day-old flies) were rapidly dissected in PBS and submitted to DNA extraction followed by quantitative real-time PCR [SyBR GreenER Supermix from lifetechnology/PCR program: 7 min at 95°C, 41× (15 s at 95°C, 1 min at 60°C)]. Specific primers for mitochondrial DNA (COXIII): 5'CGAGATGTATCACGA GAAGG/5'GAATTCCTGGAATCCTGTTG. The relative levels of mtDNA were normalized to nuclear DNA using primers to *rp49* gene: 5'GCTTCAAGATGACCATCCGCC/5'GGTGCCTTGTTCGATCC GTAAC. Normalized data were used to determine the relative levels of mtDNA molecules according to cycling threshold analysis.

Random capture mutation assay (RMC)

Twelve third-instar larvae or 3-day-old adult fly brains were rapidly dissected in PBS and immediately submitted to DNA extraction followed by *TaqI* digestion (8 h, under agitation, at 65°C/750 ng of DNA/150 units of enzyme + 150 units added after 4 h). Quantitative real-time PCR: LC FastStart DNA Master SYBR Green I kit, Roche/program: 10' at 95°C, 45× (30" at 95°C, 60" at 60°C, 15" at 72°C) + 60" at 72°C. Primers used to amplify *TaqI* site-containing DNA fragment from the *CytB* gene: 5'CCGATAGGATTATTAG ATCCTG/5'CGAACTTTACATGCTAACGGTG. These primers only amplify mtDNA fragments if the *TaqI* site has been altered by naturally occurring replication errors. The relative levels of mutated mtDNA were normalized to total mtDNA levels using primers to *COXIII* gene: 5' CGAGATGTATCACGAGAAGG/5' GAATTCCTGGAATCCTGTTG (DNA region devoid of *TaqI* site). Normalized data were used to determine the relative levels of mutated mtDNA molecules according to cycling threshold analysis.

Expanded View for this article is available online.

Acknowledgements

Imaging performed on PiCSL-FBI core facility (IBDM, AMU-Marseille) supported by French National Research Agency through "Investments for the Future" program (France-BioImaging, ANR-10-INBS-04). We thank N. Brouilly, J.P. Chauvin, and F. Richard for electron microscopy, J.M. Philippe for vectors and cloning strategies, J. Dompierre for image treatment and analysis, A. Dautant for help in protein structures analysis, C. Rubio for DNA cloning and fly culture, E. Campeau for pQCXIB plasmid, D. Chan for *MFN1/MFN2* knock-out MEFs, and L. Kerkerian-Le Goff and A. Mourier for support and critical reading of the manuscript. Stocks obtained from Bloomington *Drosophila* Stock Center (NIH P40OD018537) were used in this study. This work was supported by the Association Française contre les Myopathies (AFM-téléthon): research grant 20097 to T. Rival, PhD fellowship 16853 to N. El Fissi, and grant 17917 to M. Rojo.

Author contributions

TR initiated, conceived and supervised the project. NEF and TR performed and analyzed the experiments in *Drosophila*. AA performed electron microscopy. MR, CD, and EK performed and analyzed the experiments in mammalian cells. GP quantified PEG-fusion assay. JR provided support. TR and MR wrote the manuscript.

Conflict of interest

The authors declare that they have no conflict of interest.

References

- Murphy SM, Laura M, Fawcett K, Pandraud A, Liu YT, Davidson GL, Rossor AM, Polke JM, Castleman V, Manji H *et al* (2012) Charcot-Marie-Tooth disease: frequency of genetic subtypes and guidelines for genetic testing. *J Neurol Neurosurg Psychiatry* 83: 706–710
- Stuppia G, Rizzo F, Riboldi G, Del Bo R, Nizzardo M, Simone C, Comi GP, Bresolin N, Corti S (2015) MFN2-related neuropathies: clinical features, molecular pathogenesis and therapeutic perspectives. *J Neurol Sci* 356: 7–18
- Verhoeven K, Claeys KG, Zuchner S, Schroder JM, Weis J, Ceuterick C, Jordanova A, Nelis E, De Vriendt E, Van Hul M *et al* (2006) MFN2 mutation distribution and genotype/phenotype correlation in Charcot-Marie-Tooth type 2. *Brain* 129: 2093–2102
- Chung KW, Kim SB, Park KD, Choi KG, Lee JH, Eun HW, Suh JS, Hwang JH, Kim WK, Seo BC *et al* (2006) Early onset severe and late-onset mild Charcot-Marie-Tooth disease with mitofusin 2 (MFN2) mutations. *Brain* 129: 2103–2118
- Chung KW, Suh BC, Cho SY, Choi SK, Kang SH, Yoo JH, Hwang JY, Choi BO (2010) Early-onset Charcot-Marie-Tooth patients with mitofusin 2 mutations and brain involvement. *J Neurol Neurosurg Psychiatry* 81: 1203–1206
- Polke JM, Laura M, Pareyson D, Taroni F, Milani M, Bergamin G, Gibbons VS, Houlden H, Chamley SC, Blake J *et al* (2011) Recessive axonal Charcot-Marie-Tooth disease due to compound heterozygous mitofusin 2 mutations. *Neurology* 77: 168–173
- Piscosquito G, Saveri P, Magri S, Ciano C, Di Bella D, Milani M, Taroni F, Pareyson D (2015) Mutational mechanisms in MFN2-related neuropathy: compound heterozygosity for recessive and semidominant mutations. *J Peripher Nerv Syst* 20: 380–386
- Bertholet AM, Delerue T, Millet AM, Moulis MF, David C, Daloyau M, Arnaune-Pelloquin L, Davezac N, Mils V, Miquel MC *et al* (2016) Mitochondrial fusion/fission dynamics in neurodegeneration and neuronal plasticity. *Neurobiol Dis* 90: 3–19
- Chan DC (2012) Fusion and fission: interlinked processes critical for mitochondrial health. *Annu Rev Genet* 46: 265–287
- Westermann B (2010) Mitochondrial fusion and fission in cell life and death. *Nat Rev Mol Cell Biol* 11: 872–884
- Kawalec M, Zablocka B, Kabzinska D, Neska J, Beresewicz M (2014) Mitofusin 2 expression dominates over mitofusin 1 exclusively in mouse dorsal root ganglia - a possible explanation for peripheral nervous system involvement in Charcot-Marie-Tooth 2A. *Folia Neuropathol* 52: 436–442
- Chen H, Chomyn A, Chan DC (2005) Disruption of fusion results in mitochondrial heterogeneity and dysfunction. *J Biol Chem* 280: 26185–26192
- Chen H, Detmer SA, Ewald AJ, Griffin EE, Fraser SE, Chan DC (2003) Mitofusins Mfn1 and Mfn2 coordinately regulate mitochondrial fusion and are essential for embryonic development. *J Cell Biol* 160: 189–200
- Daumke O, Roux A (2017) Mitochondrial homeostasis: how do dimers of mitofusins mediate mitochondrial fusion? *Curr Biol* 27: R353–R356
- Otera H, Ishihara N, Mihara K (2013) New insights into the function and regulation of mitochondrial fission. *Biochem Biophys Acta* 1833: 1256–1268
- Mourier A, Motori E, Brandt T, Lagouge M, Atanassov I, Galinier A, Rappl G, Brodessa S, Hultenby K, Dieterich C *et al* (2015) Mitofusin 2 is required to maintain mitochondrial coenzyme Q levels. *J Cell Biol* 208: 429–442

17. Knott AB, Bossy-Wetzel E (2008) Impairing the mitochondrial fission and fusion balance: a new mechanism of neurodegeneration. *Ann N Y Acad Sci* 1147: 283–292
18. Grohm J, Kim SW, Mamrak U, Tobaben S, Cassidy-Stone A, Nunnari J, Plesnila N, Culmsee C (2012) Inhibition of Drp1 provides neuroprotection *in vitro* and *in vivo*. *Cell Death Differ* 19: 1446–1458
19. Burte F, Carelli V, Chinnery PF, Yu-Wai-Man P (2015) Disturbed mitochondrial dynamics and neurodegenerative disorders. *Nat Rev Neurol* 11: 11–24
20. Gerber S, Charif M, Chevrollier A, Chaumette T, Angebault C, Kane MS, Paris A, Alban J, Quiles M, Delettre C *et al* (2017) Mutations in DNML1, as in OPA1, result in dominant optic atrophy despite opposite effects on mitochondrial fusion and fission. *Brain* 140: 2586–2596
21. Kageyama Y, Zhang Z, Roda R, Fukaya M, Wakabayashi J, Wakabayashi N, Kensler TW, Reddy PH, Iijima M, Sesaki H (2012) Mitochondrial division ensures the survival of postmitotic neurons by suppressing oxidative damage. *J Cell Biol* 197: 535–551
22. Verstreken P, Ly CV, Venken KJ, Koh TW, Zhou Y, Bellen HJ (2005) Synaptic mitochondria are critical for mobilization of reserve pool vesicles at *Drosophila* neuromuscular junctions. *Neuron* 47: 365–378
23. Pham AH, Meng S, Chu QN, Chan DC (2012) Loss of Mfn2 results in progressive, retrograde degeneration of dopaminergic neurons in the nigrostriatal circuit. *Hum Mol Genet* 21: 4817–4826
24. Lee S, Sterky FH, Mourier A, Terzioglu M, Cullheim S, Olson L, Larsson NG (2012) Mitofusin 2 is necessary for striatal axonal projections of midbrain dopamine neurons. *Hum Mol Genet* 21: 4827–4835
25. Chen H, McCaffery JM, Chan DC (2007) Mitochondrial fusion protects against neurodegeneration in the cerebellum. *Cell* 130: 548–562
26. Detmer SA, Vande Velde C, Cleveland DW, Chan DC (2008) Hindlimb gait defects due to motor axon loss and reduced distal muscles in a transgenic mouse model of Charcot-Marie-Tooth type 2A. *Hum Mol Genet* 17: 367–375
27. Cartoni R, Arnaud E, Medard JJ, Poirot O, Courvoisier DS, Chrast R, Martinou JC (2010) Expression of mitofusin 2(R94Q) in a transgenic mouse leads to Charcot-Marie-Tooth neuropathy type 2A. *Brain* 133: 1460–1469
28. Strickland AV, Rebelo AP, Zhang F, Price J, Bolon B, Silva JP, Wen R, Zuchner S (2014) Characterization of the mitofusin 2 R94W mutation in a knock-in mouse model. *J Peripher Nerv Syst* 19: 152–164
29. Zuchner S, De Jonghe P, Jordanova A, Claeys KG, Guergueltcheva V, Cherninkova S, Hamilton SR, Van Stavern G, Krajewski KM, Stajich J *et al* (2006) Axonal neuropathy with optic atrophy is caused by mutations in mitofusin 2. *Ann Neurol* 59: 276–281
30. Feely SM, Laura M, Siskind CE, Sottile S, Davis M, Gibbons VS, Reilly MM, Shy ME (2011) MFN2 mutations cause severe phenotypes in most patients with CMT2A. *Neurology* 76: 1690–1696
31. Detmer SA, Chan DC (2007) Complementation between mouse Mfn1 and Mfn2 protects mitochondrial fusion defects caused by CMT2A disease mutations. *J Cell Biol* 176: 405–414
32. Malka F, Guillery O, Cifuentes-Diaz C, Guillou E, Belenguer P, Lomès M, Rojo M (2005) Separate fusion of outer and inner mitochondrial membranes. *EMBO Rep* 6: 853–859
33. Yun J, Puri R, Yang H, Lizzio MA, Wu C, Sheng ZH, Guo M (2014) MUL1 acts in parallel to the PINK1/parkin pathway in regulating mitofusin and compensates for loss of PINK1/parkin. *Elife* 3: e01958
34. Smirnova E, Griparic L, Shurland DL, van der Bliek AM (2001) Dynamin-related protein Drp1 is required for mitochondrial division in mammalian cells. *Mol Biol Cell* 12: 2245–2256
35. Park J, Lee G, Chung J (2009) The PINK1-Parkin pathway is involved in the regulation of mitochondrial remodeling process. *Biochem Biophys Res Comm* 378: 518–523
36. Banerji A, Hudry B, Sass M, Saurin AJ, Graba Y (2014) Hox proteins mediate developmental and environmental control of autophagy. *Dev Cell* 28: 56–69
37. Juhasz G, Erdi B, Sass M, Neufeld TP (2007) Atg7-dependent autophagy promotes neuronal health, stress tolerance, and longevity but is dispensable for metamorphosis in *Drosophila*. *Genes Dev* 21: 3061–3066
38. Itsara LS, Kennedy SR, Fox EJ, Yu S, Hewitt JJ, Sanchez-Contreras M, Cardozo-Pelaez F, Pallanck LJ (2014) Oxidative stress is not a major contributor to somatic mitochondrial DNA mutations. *PLoS Genet* 10: e1003974
39. Eura Y, Ishihara N, Yokota S, Mihara K (2003) Two mitofusin proteins, mammalian homologues of FZO, with distinct functions are both required for mitochondrial fusion. *J Biochem* 134: 333–344
40. Rojo M, Legros F, Chateau D, Lomès A (2002) Membrane topology and mitochondrial targeting of mitofusins, ubiquitous mammalian homologs of the transmembrane GTPase Fzo. *J Cell Sci* 115: 1663–1674
41. Cartoni R, Martinou JC (2009) Role of mitofusin 2 mutations in the physiopathology of Charcot-Marie-Tooth disease type 2A. *Exp Neurol* 218: 268–273
42. Vallat JM, Ouvrier RA, Pollard JD, Magdelaine C, Zhu D, Nicholson GA, Grew S, Ryan MM, Funalot B (2008) Histopathological findings in hereditary motor and sensory neuropathy of axonal type with onset in early childhood associated with mitofusin 2 mutations. *J Neuropathol Exp Neurol* 67: 1097–1102
43. Lv H, Wang L, Zhang W, Wang Z, Zuo Y, Liu J, Yuan Y (2015) A cohort study of Han Chinese MFN2-related Charcot-Marie-Tooth 2A. *J Neurol Sci* 358: 153–157
44. Ishihara N, Nomura M, Jofuku A, Kato H, Suzuki SO, Masuda K, Otera H, Nakanishi Y, Nonaka I, Goto Y *et al* (2009) Mitochondrial fission factor Drp1 is essential for embryonic development and synapse formation in mice. *Nat Cell Biol* 11: 958–966
45. Wakabayashi J, Zhang Z, Wakabayashi N, Tamura Y, Fukaya M, Kensler TW, Iijima M, Sesaki H (2009) The dynamin-related GTPase Drp1 is required for embryonic and brain development in mice. *J Cell Biol* 186: 805–816
46. Loiseau D, Chevrollier A, Verny C, Guillet V, Gueguen N, Pou de Crescenzo MA, Ferre M, Malinge MC, Guichet A, Nicolas G *et al* (2007) Mitochondrial coupling defect in Charcot-Marie-Tooth type 2A disease. *Ann Neurol* 61: 315–323
47. Amiot EA, Lott P, Soto J, Kang PB, McCaffery JM, DiMauro S, Abel ED, Flanigan KM, Lawson VH, Shaw JM (2008) Mitochondrial fusion and function in Charcot-Marie-Tooth type 2A patient fibroblasts with mitofusin 2 mutations. *Exp Neurol* 211: 115–127
48. Rouzier C, Bannwarth S, Chaussonnet A, Chevrollier A, Verschueren A, Bonello-Palot N, Fragaki K, Cano A, Pouget J, Pellissier JF *et al* (2012) The MFN2 gene is responsible for mitochondrial DNA instability and optic atrophy ‘plus’ phenotype. *Brain* 135: 23–34
49. Qi Y, Yan L, Yu C, Guo X, Zhou X, Hu X, Huang X, Rao Z, Lou Z, Hu J (2016) Structures of human mitofusin 1 provide insight into mitochondrial tethering. *J Cell Biol* 215: 621–629
50. Cao YL, Meng S, Chen Y, Feng JX, Gu DD, Yu B, Li YJ, Yang JY, Liao S, Chan DC *et al* (2017) MFN1 structures reveal nucleotide-triggered dimerization critical for mitochondrial fusion. *Nature* 542: 372–376

51. Koshiba T, Detmer SA, Kaiser JT, Chen H, McCaffery JM, Chan DC (2004) Structural basis of mitochondrial tethering by mitofusin complexes. *Science* 305: 858–862
52. Franco A, Kitsis RN, Fleischer JA, Gavathiotis E, Kornfeld OS, Gong G, Biris N, Benz A, Qvit N, Donnelly SK et al (2016) Correcting mitochondrial fusion by manipulating mitofusin conformations. *Nature* 540: 74–79
53. Low HH, Sachse C, Amos LA, Lowe J (2009) Structure of a bacterial dynamin-like protein lipid tube provides a mechanism for assembly and membrane curving. *Cell* 139: 1342–1352
54. Berthet A, Margolis EB, Zhang J, Hsieh I, Zhang J, Hnasko TS, Ahmad J, Edwards RH, Sesaki H, Huang EJ et al (2014) Loss of mitochondrial fission depletes axonal mitochondria in midbrain dopamine neurons. *J Neurosci* 34: 14304–14317
55. Stowers RS, Megeath LJ, Gorska-Andrzejak J, Meinertzhagen IA, Schwarz TL (2002) Axonal transport of mitochondria to synapses depends on Milton, a novel *Drosophila* protein. *Neuron* 36: 1063–1077
56. Ma H, Cai Q, Lu W, Sheng ZH, Mochida S (2009) KIF5B motor adaptor syntabulin maintains synaptic transmission in sympathetic neurons. *J Neurosci* 29: 13019–13029
57. Guo X, Macleod GT, Wellington A, Hu F, Panchumarthi S, Schoenfield M, Marin L, Charlton MP, Atwood HL, Zinsmaier KE (2005) The GTPase dMiro is required for axonal transport of mitochondria to *Drosophila* synapses. *Neuron* 47: 379–393
58. Sheng ZH, Cai Q (2012) Mitochondrial transport in neurons: impact on synaptic homeostasis and neurodegeneration. *Nat Rev Neurosci* 13: 77–93
59. Braathen GJ, Hoyer H, Busk OL, Tveten K, Skjelbred CF, Russell MB (2016) Variants in the genes DCTN2, DNAH10, LRIG3, and MYO1A are associated with intermediate Charcot-Marie-Tooth disease in a Norwegian family. *Acta Neurol Scand* 134: 67–75
60. Eschbach J, Sinniger J, Bouitbir J, Fergani A, Schlagowski AI, Zoll J, Geny B, Rene F, Larmet Y, Marion V et al (2013) Dynein mutations associated with hereditary motor neuropathies impair mitochondrial morphology and function with age. *Neurobiol Dis* 58: 220–230
61. Twig G, Elorza A, Molina AJ, Mohamed H, Wikstrom JD, Walzer G, Stiles L, Haigh SE, Katz S, Las G et al (2008) Fission and selective fusion govern mitochondrial segregation and elimination by autophagy. *EMBO J* 27: 433–446
62. Frank M, Duvezin-Caubet S, Koob S, Occhipinti A, Jagasia R, Petcherski A, Ruonala MO, Priault M, Salin B, Reichert AS (2012) Mitophagy is triggered by mild oxidative stress in a mitochondrial fission dependent manner. *Biochem Biophys Acta* 1823: 2297–2310
63. Lee Y, Lee HY, Hanna RA, Gustafsson AB (2011) Mitochondrial autophagy by Bnip3 involves Drp1-mediated mitochondrial fission and recruitment of Parkin in cardiac myocytes. *Am J Physiol Heart Circ Physiol* 301: H1924–H1931
64. Sauvanet C, Duvezin-Caubet S, Salin B, David C, Massoni-Laporte A, di Rago JP, Rojo M (2012) Mitochondrial DNA mutations provoke dominant inhibition of mitochondrial inner membrane fusion. *PLoS One* 7: e49639
65. Yue W, Chen Z, Liu H, Yan C, Chen M, Feng D, Yan C, Wu H, Du L, Wang Y et al (2014) A small natural molecule promotes mitochondrial fusion through inhibition of the deubiquitinase USP30. *Cell Res* 24: 482–496
66. Low HH, Lowe J (2006) A bacterial dynamin-like protein. *Nature* 444: 766–769
67. Zhang Y, Skolnick J (2005) TM-align: a protein structure alignment algorithm based on the TM-score. *Nucleic Acids Res* 33: 2302–2309
68. Sage D, Donati L, Soulez F, Fortun D, Schmit G, Seitz A, Guet R, Vonesch C, Unser M (2017) DeconvolutionLab2: an open-source software for deconvolution microscopy. *Methods* 115: 28–41
69. Bolte S, Cordelieres FP (2006) A guided tour into subcellular colocalization analysis in light microscopy. *J Microsc* 224: 213–232
70. Chudakov DM, Lukyanov S, Lukyanov KA (2007) Tracking intracellular protein movements using photoswitchable fluorescent proteins PS-CFP2 and Dendra2. *Nat Protoc* 2: 2024–2032
71. Sandoval H, Yao CK, Chen K, Jaiswal M, Danti T, Lin YQ, Bayat V, Xiong B, Zhang K, David G et al (2014) Mitochondrial fusion but not fission regulates larval growth and synaptic development through steroid hormone production. *Elife* 3: e03558
72. Owusu-Ansah E, Yavari A, Mandal S, Banerjee U (2008) Distinct mitochondrial retrograde signals control the G1-S cell cycle checkpoint. *Nat Genet* 40: 356–361